Click Here for Full Article

Imaging mantle discontinuities using least squares Radon transform

Yuling An,[1] Yu Jeffrey Gu,[1] and Mauricio D. Sacchi[1]

[1] Differential traveltimes of *SS* precursors have been widely used to map large-scale mantle structure and depths of discontinuities. Measurements are commonly made by stacking individual records to increase the signal-to-noise ratio pertaining to these mild reflections. However, ray parameters of the *SS* precursors are typically less well constrained and undesired seismic arrivals with vastly different slownesses (for example, scattered waves) could potentially contaminate the time domain stacks. To overcome these pitfalls, we introduce a processing scheme based on the Radon transform and well-constrained inversions. Our method is particularly effective in suppressing background noise, constraining differential ray parameter and traveltime, and detecting weak reflected or converted phases. We apply the Radon-based method to delineate the discontinuity structure beneath the northeastern Pacific Ocean and the northwestern Canada. An elevated 410-km discontinuity and a thickened transition zone (252 km) are observed beneath the northern British Columbia, which may be caused by remnant oceanic lithosphere from the subduction of Kula-Farallon plate under North America. A thin transition zone is identified beneath the northern Pacific Ocean and its presence is supported by a low shear-velocity anomaly from recent tomographic models. The improved accuracy and resolution using the least squares Radon transform also offer clear evidence for a regional 520-km discontinuity and several mild reflectors in the depth ranges of 250–330 km and 900–1200 km. We do not observe a 220-km discontinuity beneath the study region.
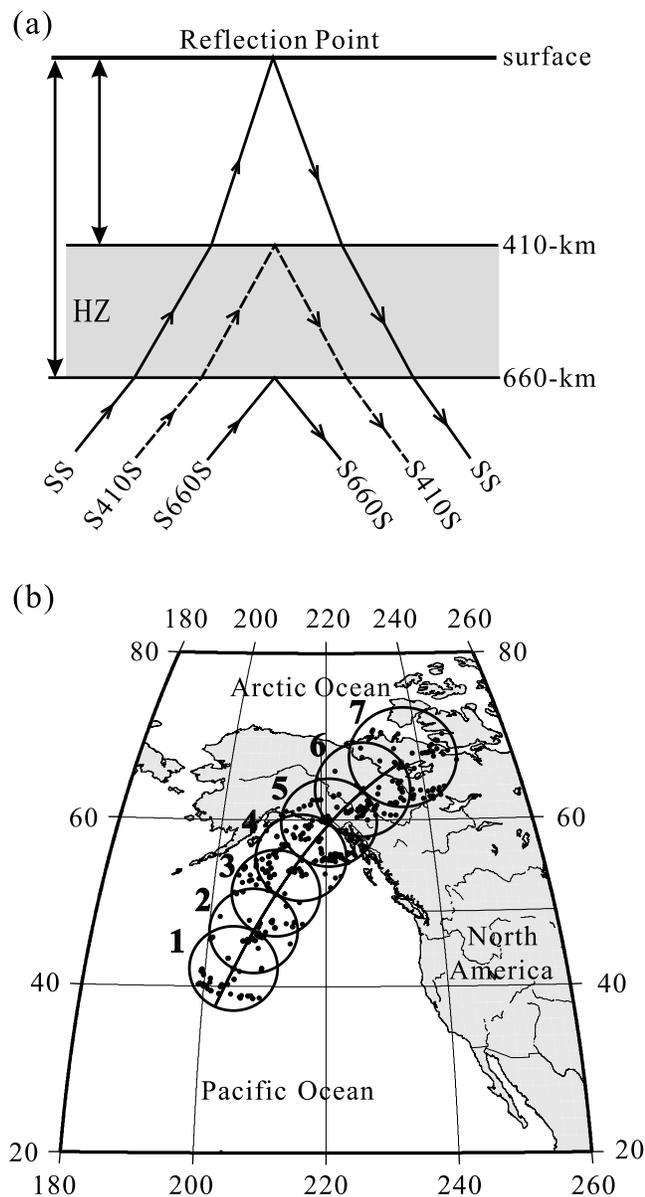
1. Introduction

[2] The existence and the characteristics of seismic discontinuities have been widely used as effective tracers of thermal and compositional variations in the mantle. Among the most robust observations, the 410- and 660-km discontinuities have been shown to exist globally [e.g., *Shearer and Masters*, 1992; *Shearer*, 1993; *Gossler and Kind*, 1996; *Flanagan and Shearer*, 1998; *Gu et al.*, 1998; *Flanagan and Shearer*, 1999; *Gu and Dziewonski*, 2002; *Chambers et al.*, 2005] and their lateral depth variations potentially reflect the local pressure-temperature conditions under which olivine phase transitions take place [*Ringwood*, 1975; *Agee and Walker*, 1988; *Katsura and Ito*, 1989]. Temperature perturbations, which can cause tens of kilometers of topography on a given discontinuity, have been reported both on local and global scales [*Gossler and Kind*, 1996; *Gu et al.*, 1998; *Deuss and Woodhouse*, 2002]. Other seismic discontinuities/reflectors are only intermittently reported and remain controversial, most notably near 220-km (largely continental) [*Gu et al.*, 2001; *Deuss and Woodhouse*, 2002], 250–350 km [*Revenaugh and Jordan*,

1991; *Deuss and Woodhouse*, 2002], 500–600 km (global) [e.g., *Shearer*, 1990; *Deuss and Woodhouse*, 2001], and 900–1200 km [*Kawakatsu and Niu*, 1994; *Niu and Kawakatsu*, 1997]. Each of them represents a potential piece of the puzzle in the accurate description of the subsurface thermal and compositional regimes.

[3] Global constraints of mantle discontinuities mainly come from long-period waves, despite the increasing popularity of higher-frequency method such as receiver functions in recent years. Of the methods based on long-period waves, *SS* precursors remain one of proven means for identifying and interpreting mantle reflectors [e.g., *Shearer and Master*, 1992; *Shearer*, 1993; *Gossler and Kind*, 1996; *Gu et al.*, 1998; *Flanagan and Shearer*, 1998; *Gu and Dziewonski*, 2002; *Schmerr and Garnero*, 2006]. These weak underside reflections are highly sensitive to both depth and reflectivity of mantle reflectors but, to a much less extent, to the station location.

[4] Among techniques used in analyzing *SS* precursors, waveform stacking of data at similar geographical locations (or 'bins') is commonly used to enhance signal-to-noise ratio [e.g., *Shearer*, 1993]. Occasional variations in identifying and differentiating these weak seismic phases include stacking along a given slowness [*Gossler and Kind*, 1996; *Gu et al.*, 1998] or back azimuth (the ''vespa'' technique) [*Rost and Thomas*, 2002]. Most of these methods are time

---

[1]University of Alberta, Edmonton, Alberta, Canada.

Figure 1. (a) Ray geometries of *SS* and its precursors. (b) The position of study area. There are seven 5-deg caps across the northeastern Pacific Ocean and the northwestern Canada. The black dots denote the reflection points of *SS*.

long-period *SS* precursors; second, to delineate all possible seismic discontinuities across the northeastern Pacific Ocean and the northwestern Canada. Our study region is particularly well sampled by *SS* reflection points in the distance range from 100° to 160°. Tectonically, our region encompasses landmasses of intermediate-to-young oceanic lithosphere, accretionary margins, and stable continental platforms. The diverse tectonic signatures invite a number of important scientific questions regarding the presence and nature of seismic discontinuities in the mantle. We present regional observations and interpretations for all mantle discontinuities below 200 km to address, at least partially, some of the above questions. Our results reveal strong thermal variations beneath the selected profile and provide a glimpse of the uncanny potential of the *least squares* Radon transform in mapping subsurface structures.

2. Data Selection and Preprocessing

2.1. Data Selection

[6] In this study, we analyze *SS* precursors — weak underside reflections from mantle interfaces that are strongly sensitive to the structure near the midpoint of the raypath (Figure 1a). We utilize more than ten years of long-period broadband data archived by GDSN, IRIS, GEOSCOPE and other seismic networks. To ensure the quality of our data set, we select records from shallow events (<45 km) to minimize the interference from depth phases (e.g., *sSS*). We only consider events with magnitude greater than 5.0 (Mw) to ensure good signal-to-noise ratio (from now on, SNR), and restrict the epicentral distance to 100°-160° to minimize waveform interference from topside reflection *sdsS* and *ScS* precursors *ScSdScS*, where *d* denotes a discontinuity [*Schmerr and Garnero*, 2006]. We apply a Buttersworth band-pass filter with corner periods at 15 s and 75 s. The filtered data are subjected to a SNR-based selection criterion (defined by the ratio between *SS* and its proceeding "noise" level); all records with SNR lower than 3.0 are automatically rejected. We improve the data quality further by interactively inspecting all seismograms using a MATLAB-based visualization and stacking code. The polarity of a given seismogram is reversed if necessary to account for potential instrument misorientations.

[7] After the selection steps outlined above, we are able to retrieve 402 high-quality records. We divide these data set into seven 5-deg radius spherical bins along the great circle, connecting (155.335°W, 42.098°N) and (124.189°W, 66.859°N) (Figure 1b). The bin size is dictated partly by the number of data for an effective analysis, and partly by the size of Fresnel zone (∼1000 km for a 130-deg, 20 s *SS* wave). The overlap between any two bins introduces coherent spatial averaging across our study transact.

2.2. Corrections

[8] To equalize the source, we align the first major swing of the reference pulse *SS* and normalize each record by its maximum absolute amplitude. We then multiply each record by the square root of its SNR to increase the weight of high-quality records. After alignment and normalization, we account for the effect of surface topography, crust

domain, forward analysis of waveforms. In this study, we introduce a damped least squares inversion approach based on the Radon transform to provide more accurate, high-resolution solutions for differential traveltimes and ray parameters of *SS* precursors. This method also provides an effective mechanism to resample the data in space domain. While similar approaches have been used in focusing the energy of shallow seismic signals and attenuating correlated/random noise [*Hampson*, 1986; *Foster and Mosher*, 1992], their potential applications in global seismology are still thinly explored [*Wilson and Guitton*, 2007].

[5] Our study has two main objectives: first, to assess the effectiveness of the Radon-based method for the analysis of

thickness and mantle heterogeneity. The effects of surface topography and crust thickness at the reflection point are computed from ETOPO5 (distributed by National Geophysical Data Center) and CRUST2.0 [*Bassin and Laske*, 2000], respectively. The heterogeneity correction is computed from S12_WM13 [*Su et al.*, 1994]. We do not correct for epicentral distance as did in earlier studies of *SS* precursors [e.g., *Shearer*, 1993; *Gu et al.*, 1998; *Flanagan and Shearer*, 1998; *Duess and Woodhouse*, 2002] since the distance-time relationship is an integral part of the Radon analysis.

3. Radon Transform

3.1. Theory

[9] The Radon transform (RT) is widely used in reflection seismology for hydrocarbon exploration to attenuate undesired signals, such as multiples, source generated noise, and surface waves [*Hampson*, 1986]. In this paper, the Radon transform is used to improve the SNR of *SS* precursors.

[10] Let $d(t, x_k)$, $k = 1, N$ represents a suite of N seismograms. The variable x_k indicates the distance or relative range of the k-th seismogram. The Radon transform is a simple integration of the data along a family of parametric lines $t = \tau + px$, where p indicates the ray parameter or local dip of the waveform in the spatial window of analysis; the variable τ indicates the intercept time or, in other words, the time of a linear event at $x = 0$.

Mathematically, the Radon transform is represented as follows:

$$\tilde{u}(\tau, p) = \sum_{k=1}^{N} d(t = \tau + p\, x_k, x_k). \quad (1)$$

The data in the transformed domain, $\tilde{u}(\tau, p)$ is often referred to as the $\tau - p$ signal. Equation (1) represents the low resolution Radon transform (or slowness slant stacks) that can be used to search for seismic arrivals with linear move out. In addition, it can be interpreted as a transformation that maps a linear waveform in $t - x$ domain to a point in $\tau - p$ domain, which is true if we assume an array of infinite aperture. In order to build a strategy for SNR enhancement, we require a transformation that is able to model the data. Rather than using equation (1), we adopt the following expression which is often called the forward Radon transform:

$$d(t, x_k) = \sum_{j=1}^{M} u(\tau = t - p_j x_k, p_j), \ k = 1, \ldots, N. \quad (2)$$

By adopting expression (2), we are able to represent the data as a linear superposition of signals in the $\tau - p$ domain. The advantage of equation (2) is that we can consider the Radon transform as an inverse problem to estimate the $\tau - p$ model and, after filtering, use the forward Radon transform to reconstruct the data. In addition, the part of the data not modeled by the transform can be incorporated into the formulation as follows:

$$d(t, x_k) = \sum_{j=1}^{M} u(\tau = t - p_j x_k, p_j) + e(t, x_k), \ k = 1, \ldots, N. \quad (3)$$

The error term $e(t, x_k)$ accounts not only for noise but also for undesired scattered waveforms that are not modeled by the forward Radon operator.

3.2. Inversion of the Forward Radon Transform in Frequency Domain

[11] In this section we present a technique to invert equation (3). By applying the Fourier transform with respect to the temporal variable t to both sides of expression (3) and by using the Fourier delay theorem [*Papoulis*, 1962], expression (3) reduces to the following:

$$D(f, x_k) = \sum_{j=1}^{M} U(f, p_j) e^{-i2\pi f x_k p_j} + E(f, x_k), k = 1, \ldots, N. \quad (4)$$

Expression (4) can be expanded as follows:

$$\begin{pmatrix} D(f, x_1) \\ D(f, x_2) \\ . \\ . \\ . \\ D(f, x_N) \end{pmatrix} = \begin{pmatrix} e^{-i2\pi f x_1 p_1} & e^{-i2\pi f x_1 p_2} & . & e^{-i2\pi f x_1 p_M} \\ e^{-i2\pi f x_2 p_1} & e^{-i2\pi f x_2 p_2} & . & e^{-i2\pi f x_2 p_M} \\ . & . & . & . \\ . & . & . & . \\ . & . & . & . \\ e^{-i2\pi f x_N p_1} & e^{-i2\pi f x_N p_2} & . & e^{-i2\pi f x_N p_M} \end{pmatrix} \begin{pmatrix} U(f, p_1) \\ U(f, p_2) \\ . \\ . \\ . \\ U(f, p_M) \end{pmatrix} + \begin{pmatrix} E(f, x_1) \\ E(f, x_2) \\ . \\ . \\ . \\ E(f, x_N) \end{pmatrix}. \quad (5)$$

To avoid notational clutter, we rewrite equation (5) using a matrix notation:

$$\mathbf{D}(f) = \mathbf{L}(f)\, \mathbf{U}(f) + \mathbf{E}(f). \quad (6)$$

It is clear that for a single monochromatic frequency f, we have reduced our problem to a linear inverse problem. Equation (6) is solved using the damped least squares (DLS) method [*Menke*, 1989]. The DLS method finds the minimum of the following cost function:

$$J(f) = \| \mathbf{L}(f)\mathbf{U}(f) - \mathbf{D}(f) \|_2^2 + \mu \| \mathbf{U}(f) \|_2^2. \quad (7)$$

The first term in the right hand side is the data misfit, a measure of how well the forward Radon operator can model the data. The second term is the regularization term (also known as damping or penalty term) which is required to stabilize the solution. We have also introduced a trade-off parameter μ to control the fidelity to which the forward Radon operator can model the data. The DLS solution is found by minimizing equation (7) with respect to the

unknown solution vector $\mathbf{U}(f)$. It is easy to show that the minimum of (7) is given by

$$\mathbf{U}(f) = \left(\mathbf{L}^H(f)\mathbf{L}(f) + \mu\mathbf{I}\right)^{-1}\mathbf{L}^H(f)\mathbf{D}(f), \qquad (8)$$

where H represents the conjugate transpose operator. It is important to stress that equation (8) must be solved for all frequencies f. Once $\mathbf{U}(f)$ is obtained for all frequencies, we use the inverse Fourier transform to map $U(f, p_j)$ to time domain. The final result is the Radon operator $u(\tau, p_j)$ in time domain and we refer to the above procedure as the damped least squares Radon transform (from here on, LSRT).

[12] It is important to note that several strategies to invert equation (6) exist. We have adopted the DLS method but other non-quadratic regularization methods could have also been adopted [*Sacchi and Ulrych*, 1995; *Wilson and Guitton*, 2007], that enables, the latter allows, under good SNR conditions, for high resolution Radon transforms. In other words, it represents a Radon transform where the artifacts introduced by limited aperture are attenuated. The application of high-resolution Radon transforms for pre-processing and filtering *SS* precursors is presently considered as an alternative.

3.3. Radon Filtering and Data Re-sampling

[13] We now have two operators: one to compute the Radon transform, the other to reconstruct the data. In other words, we have a pair of transforms:

$$\begin{cases} \mathbf{U}(f) = \left(\mathbf{L}^H(f)\mathbf{L}(f) + \mu\mathbf{I}\right)^{-1}\mathbf{L}^H(f)\mathbf{D}(f) \\ \hat{\mathbf{D}}(f) = \mathbf{L}(f)\mathbf{U}(f) \end{cases}, \qquad (9)$$

where that the reconstructed data are indicated by $\hat{\mathbf{D}}(f)$. The inverted Radon transform can be filtered to exclude undesired ray-parameters before mapping the data back to the spatial domain. In addition, one can use two different operators to evaluate the Radon Transform, 1) with the original data aperture $\mathbf{L}_o(f)$, and 2) to the new spatial positions $\mathbf{L}_r(f)$ to re-sample the data. The pair of operators is given by

$$\begin{cases} \mathbf{U}(f) = \left(\mathbf{L}_o^H(f)\mathbf{L}_o(f) + \mu\mathbf{I}\right)^{-1}\mathbf{L}_o^H(f)\mathbf{D}(f) \\ \hat{\mathbf{D}}(f) = \mathbf{L}_r(f)\mathbf{U}(f) \end{cases}. \qquad (10)$$

Equation (10) is used to interpolate data in the examples provided in the following sections.

3.4. Synthetic Tests

[14] The formulation of the Radon transform provides mechanisms for signal enhancement, noise attenuation and interpolation. First, by adjusting the trade-off parameter, one can control the degree of fitting of the original data to the data generated with the forward Radon operator. Second, once a $\tau - p$ model is obtained, the forward transform can be applied to reproduce the time domain data, as well as to resample and interpolate them. Spatial interpolation is particularly useful considering that gaps in data coverage are often prevalent in earthquake recordings. Finally, the Radon transform can be used to remove interfering arrivals with vastly different $\tau - p$ values by filtering the data in the Radon domain. These properties make the Radon transform effective in differentiating small seismic phases of interest from random noise or scattered waveforms.

[15] It is possible to compute the Radon transform by directly using equation (1) to produce slowness slant stacks. However, the LSRT inversion procedure outlined in section 3.2 (equation 8) provides solutions with higher resolution than the standard slant stacking approach. LSRT also enables the reconstruction of the time series, which is a distinct advantage over traditional time domain delay-and-sum.

[16] Figure 2 compares the Radon solutions obtained from LSRT (equation 8) with those from slowness slant stacks (equation 1) using synthetic records. The input time domain traces shown in Figure 2a contain four seismic arrivals with linear distance-time relationships. We add random noise to each trace to simulate data under realistic conditions. The resulting $\tau - p$ model obtained from LSRT (Figure 2b) shows four narrowly focused maxima that are highly consistent with those of the input records. In comparison, the resolution of the $\tau - p$ model obtained using equation (1) (Figure 2c) is visibly lower, though the resulting $\tau - p$ values are highly consistent with those obtained using LSRT.

[17] Figure 2d shows reconstructed time series using the solutions from LSRT; the results after resampling and interpolation are shown in Figure 2e. We follow a standard procedure and choose the turning point of the L-curve [*Engl and Grever*, 1994] as the trade-off parameter. The inverse problem is solved in the frequency domain, and the misfit $\left(\sum_f |L(f)U(f) - D(f)|^2\right)$ and model norm $\left(\sum_f |U(f)|^2\right)$ for all frequencies are displayed in Figure 2f. In our example, the turning point occurs at approximately $\mu = 18$.

3.5. Robustness Test With Synthetic SS Precursors

[18] The *SS* precursor data set is more complicated than the simulated data set examined in section 3.4. Since each record has been aligned to *SS*, the traveltimes of the remaining phases become relative (or corrected) times to *SS*; similarly, the ray parameters of the remaining phases become differential ray parameters to that of *SS*. To determine suitable RT algorithm for this data set, we first fit the theoretical relative traveltimes of *S220S*, *S410S* and *S660S* (generated from PREM) using 2nd order polynomials (Figure 3a). These traveltime curves are approximately linear and the coefficients of quadratic terms are about

---

Figure 2. (a) Simulated data with four reflections. (b) Radon domain signals of the simulated data shown as energy envelopes. Four focused maxima precisely represent the reflections in Figure 2a. (c) The low resolution Radon signals computed from equation (1) and shown as energy envelopes. The thick solid lines in (b) and (c) show an energy value of 0.6. (d) Reconstructed data with the Radon operator presented in Figure 2b. (e) The predicted data after resampling and interpolation. (f) Trade-off diagram (L-curve) for choosing the optimal damping parameter.
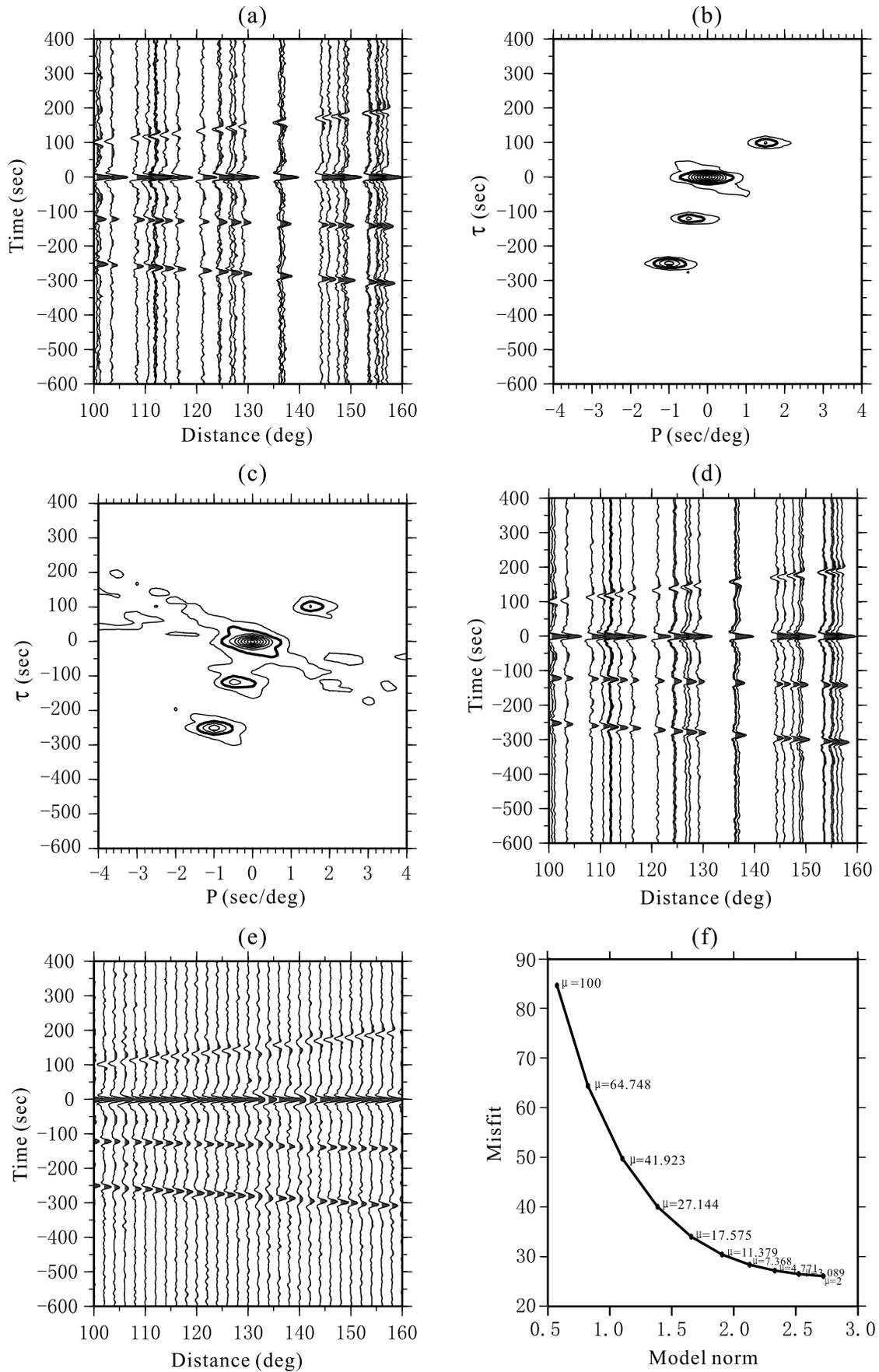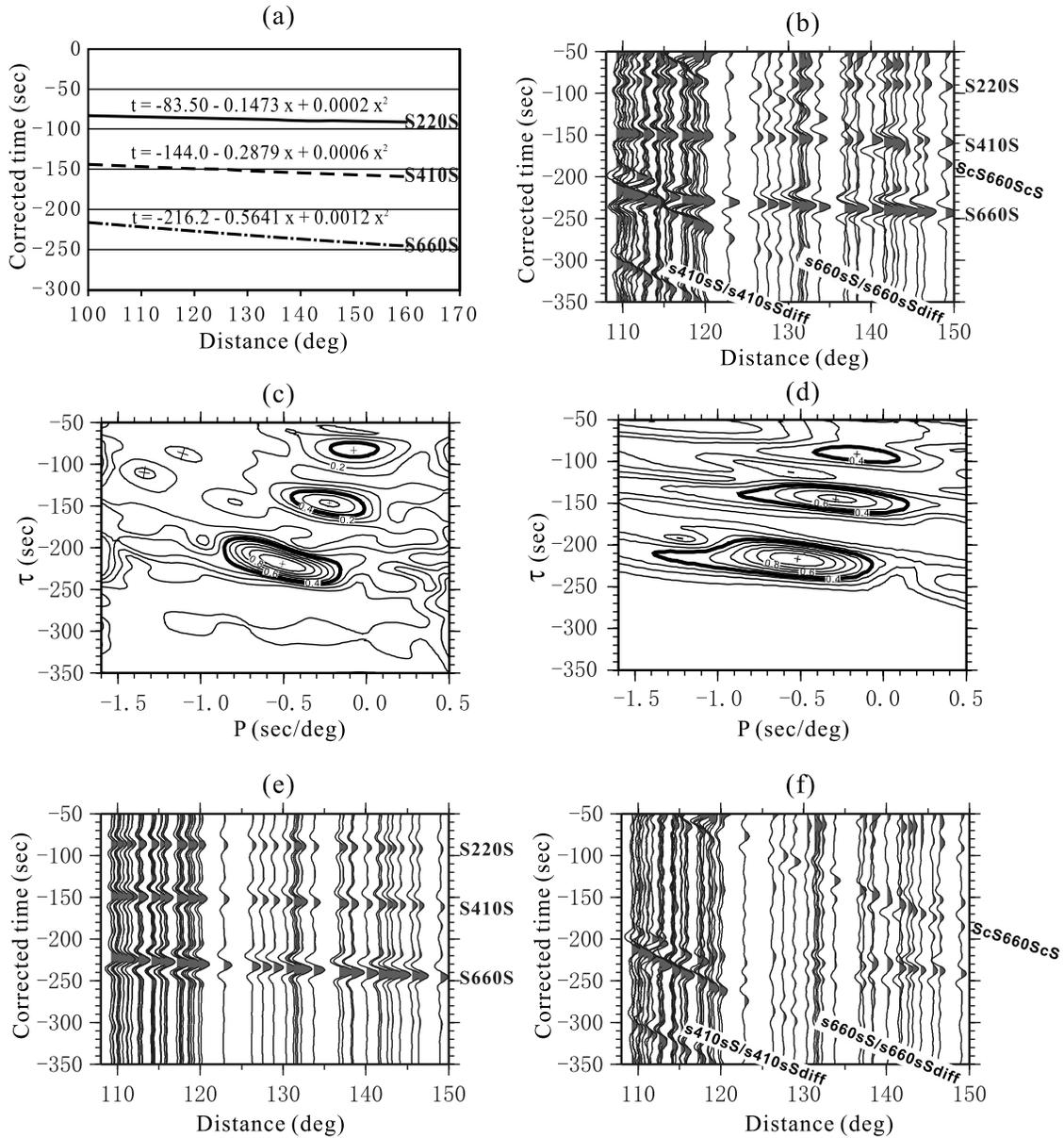
Figure 2

Figure 3. (a) Corrected traveltime curves of SS precursors, calculated based on PREM. (b) Synthetic seismograms computed using PREM for cap7 after aligning on and normalizing by SS. (c) The Radon-domain signals (shown as energy envelope) for the synthetic seismograms. (d) The low resolution Radon signals computed from equation (1). The thick solid lines denote the energy value of 0.4. (e) The reconstructed time series with the Radon operator shown in (c). Undesired reflections and random noise are strongly attenuated. (f) The residual between the original and reconstructed time series.

500 times smaller than those of the respective linear terms. We keep the quadratic term by adopting an empirical scaling factor and write the traveltime equation as follows:

$$t = \tau + px + \alpha px^2, \qquad (11)$$

where $\alpha = -0.002$ is the scaling factor, x is the distance in $t - x$ domain, τ is the intercept time in $\tau - p$ domain, and p is the relative ray parameter to that of SS.

[19] Figure 3b shows the synthetic seismograms after aligning on and normalizing by SS for cap 7. These seismograms are computed based on PREM using a mode summation approach. Arrivals resulting from the underside reflections of 220-, 410- and 660-km discontinuities are clearly identified. The Radon model after applying LSRT based on equations (8) and (11) (Figure 3c) recovers three well-defined energy maxima with relative p values of −0.10, −0.226 and −0.502 deg/sec, corresponding to S220S, S410S and S660S, respectively. The intercept time τ is the relative traveltime to SS at 100° epicentral distance. Figure 3d shows the Radon signals (shown as energy envelopes) calculated from slowness slant stacks. The measurements of τ values from the energy maxima are consistent between Figures 3c and 3d, and their resolutions
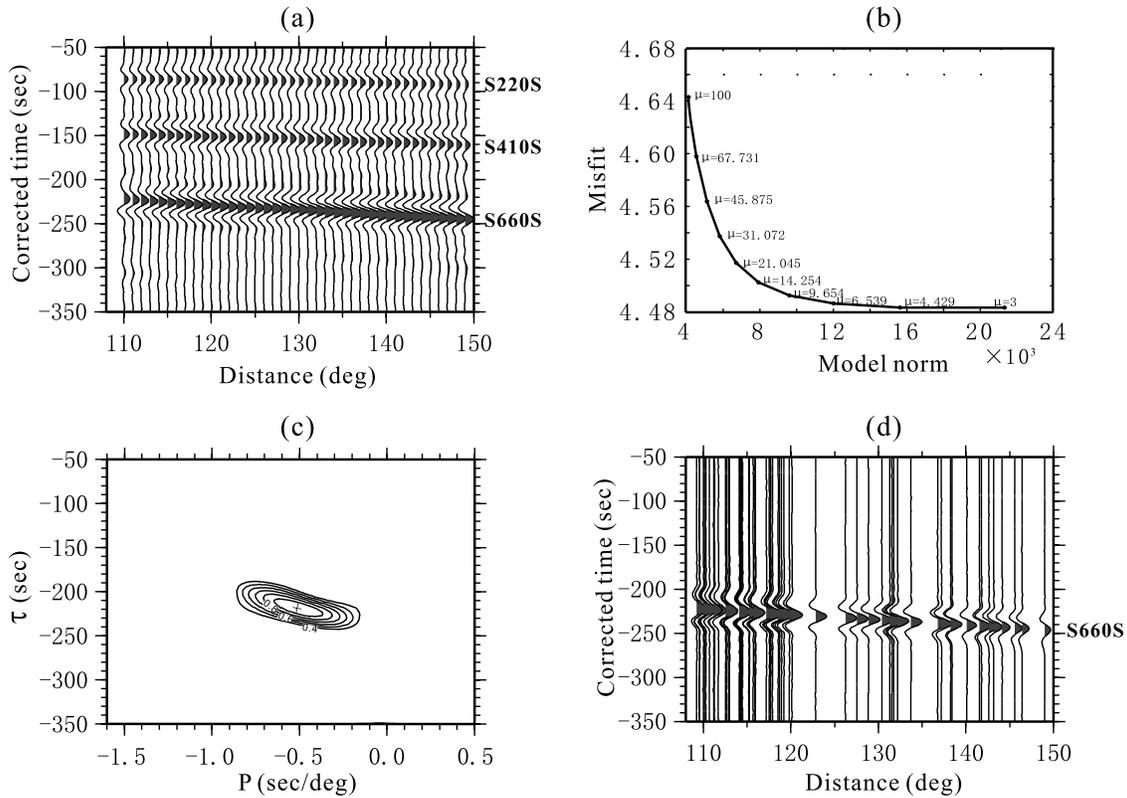
Figure 4. (a) Reconstructed time series after resampling and spatial interpolation. (b) The trade-off curve for choosing the optimal damping parameter μ. In this case, the optimal value for μ is 21. (c) An isolated $\tau - p$ signal for S660S after the Radon-domain windowing. (d) The reconstructed time series from the Radon operator shown in Figure 4c.

are comparable. However, the resolution of the ray parameter is substantially improved by LSRT (see Figure 3c). Again, the $\tau - p$ model shown in Figure 3c can be used to reconstruct data in the time domain (Figures 3e). The residual plot (Figure 3f) shows clear $ScSdScS$ and $sdsS/sdsS_{diff}$ move outs; the ability to eliminate such interfering arrivals outside the $\tau - p$ range of interest is a key advantage of LSRT.

[20] Figure 4a shows the reconstructed time domain signals based on LSRT after spatial resampling and interpolation. The interpolated time series are clearly superior in quality than the original data due to the removal of noise and gaps in data coverage. The extent of filtering and smoothing are determined using the L-curve (Figure 4b). Additional post-inversion processing techniques can be applied to isolate the time domain signal of interest, for example, one could filter the $\tau - p$ image (Figure 4c) prior to time series reconstruction to extract a stand-alone signal for $S660S$ (Figure 4d).

3.6. RT of Broadband SS Precursors

[21] In theory, the Radon transform can be directly applied to the reflections and conversions from mantle discontinuities. In practice, however, the recorded SS precursors often require additional signal enhancement due to the presence of correlated/random noise and incomplete data coverage. Figure 5a shows the preprocessed data from cap 7 where $S410S$ and $S660S$ are nearly indistin-

guishable from the surrounding noise. Without preconditioning, the LSRT cannot effectively collapse the time domain reflections to $\tau - p$ values; the scatter in the Radon domain is as severe as it is in time domain (Figure 5b). The RT model-predicted data with (Figure 5c) and without (Figure 5d) resampling show little, if any, improvement over the original time series.

[22] We precondition the data by partially stacking SdS along the theoretical traveltime curve calculated using PREM [Dziewonski and Anderson, 1981] for a selected distance window. The window size dictates the amount of smoothing and the net result is an effective running average of records within a window. Our adopted window size of $20°-30°$ is superior to common approaches such as slowness stacking (that typically averages the entire distance range; see Gossler and Kind, 1996) and strikes a reasonable balance between signal coherence and data resolution.

[23] Figure 6a shows the partially stacked traces of the original data (see Figure 5a) with a spatial averaging distance of $20°$. For the LSRT approach, the improvement of SNR in the time domain substantially enhances energy focusing in the Radon domain (Figure 6b). We identify peaks at $\tau - p$ values of (-143.60 sec, -0.206 sec/deg) and (-212.96 sec, -0.505 sec/deg) for $S410S$ and $S660S$, respectively. These values vary slightly from the PREM predictions (denoted by solid black dots in Figure 6b) as well as from the lower resolution slowness slant stacks
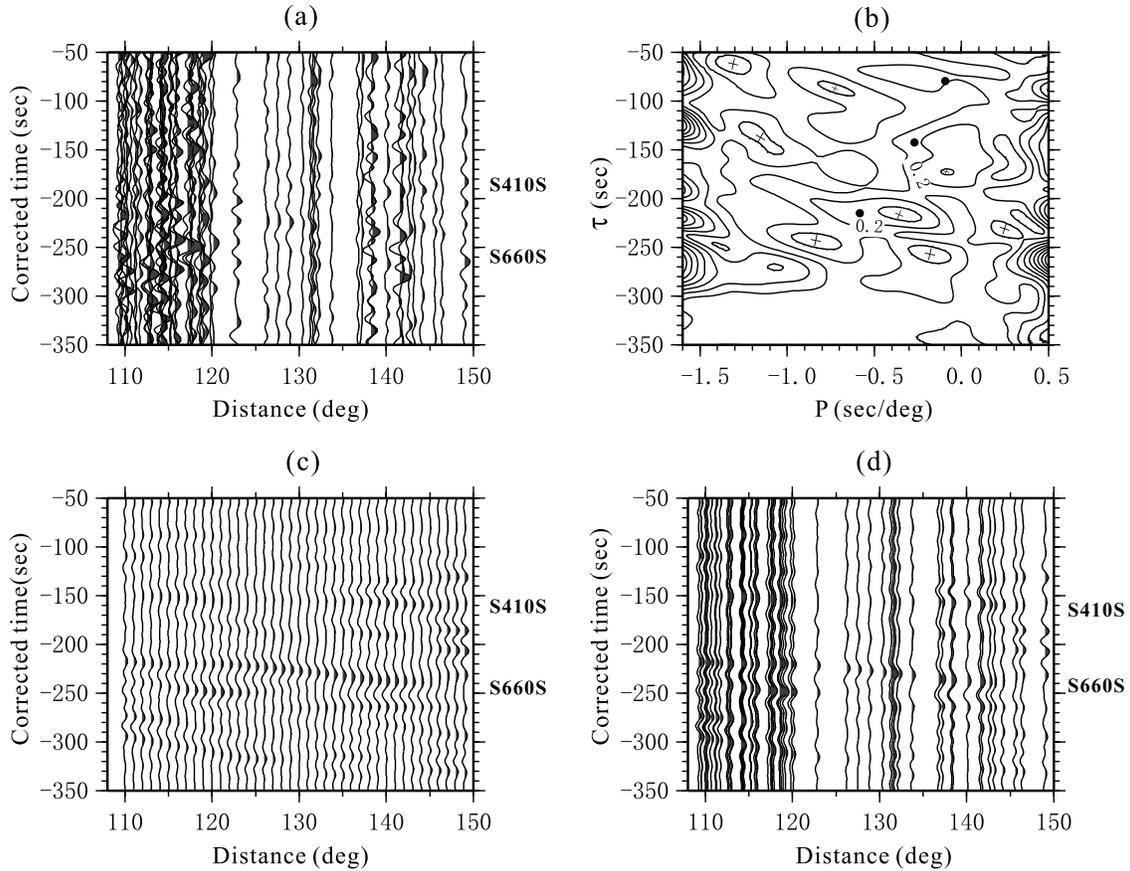
Figure 5. (a) Unconditioned time series from cap 7. The reflections from mantle discontinuities are buried in the background noise. (b) The Radon-domain equivalent of Figure 5a. No recognizable pattern is detected. The black dots denote the theoretical $\tau - p$ values for S220S, S400S, and S670S from PREM. (c) The reconstructed data after resampling and spatial interpolation. (d) The reconstructed time series.

(Figure 6c). The traveltime curves presented by the reconstructed (Figure 6d) and spatially resampled (Figure 6e) time series are consistent with those of the original, partially stacked data. Two weaker signals are present, which are likely associated with secondary discontinuities in the mantle.

4. Mapping Mantle Discontinuities

4.1. Radon Inversions

[24] We perform LSRT to seven 5-deg caps and tabulate the corrected intercept time τ and relative ray parameter p in Table 1. The intercept time τ represents the distance-corrected differential traveltime of $SdS - SS$ at 100°. For partial stacking, we choose an averaging distance of 30° for the first two caps (Figure 7) and 20° for the remaining caps. These values of τ and p are stable for a wide range of smoothing parameters and the main features are only weakly affected by the choice of mantle velocity model. The observed $\tau - p$ deviations from those of synthetic seismograms reflect the arrival time perturbations relative to the PREM model. To ensure correctness, we analyze $S410S$ and $S660S$ separately and compare the partially stacked time series (left column, Figures 7 and 8) with the corresponding energy diagram in the Radon domain (right column, Figures 7 and 8). In most cases, distinct Radon

peaks accurately reflect the various secondary arrivals proceeding SS. More importantly, coherent phases outside of the interest of this study, for example, the topside reflections $sdsS$ and ScS multiples, are effectively eliminated from the original time series through Radon-domain windowing.

4.2. Depth of TZ Discontinuities

[25] The differential traveltimes between the observed and PREM-based SS precursors represent depth perturbations of mantle discontinuities. We compute theoretical times for SS and SdS for a range of depths and determine the depth that best matches the observed τ values. We stack the reconstructed data/synthetic seismograms along the best fit traveltime curves and collapse to one representative distance of 100° (Figures 9a and 9b). Figure 10 compares our migrated depth estimates of TZ discontinuities with those from *Flanagan and Shearer* [1998] and *Gu et al.* [2003] at similar locations. Our depths span 29 km for 410-km discontinuity (391−420 km) and 33 km for 660-km discontinuity (634−667 km) (see Table 1), both are notably larger than the reported variations from earlier studies along similar transects. The regional average depths of 412.1 km and 648.1 km agree well with the corresponding values from *Gu et al.* [2003] and are only slightly shallower than those of *Flanagan and Shearer* [1998]. The 410-km dis-
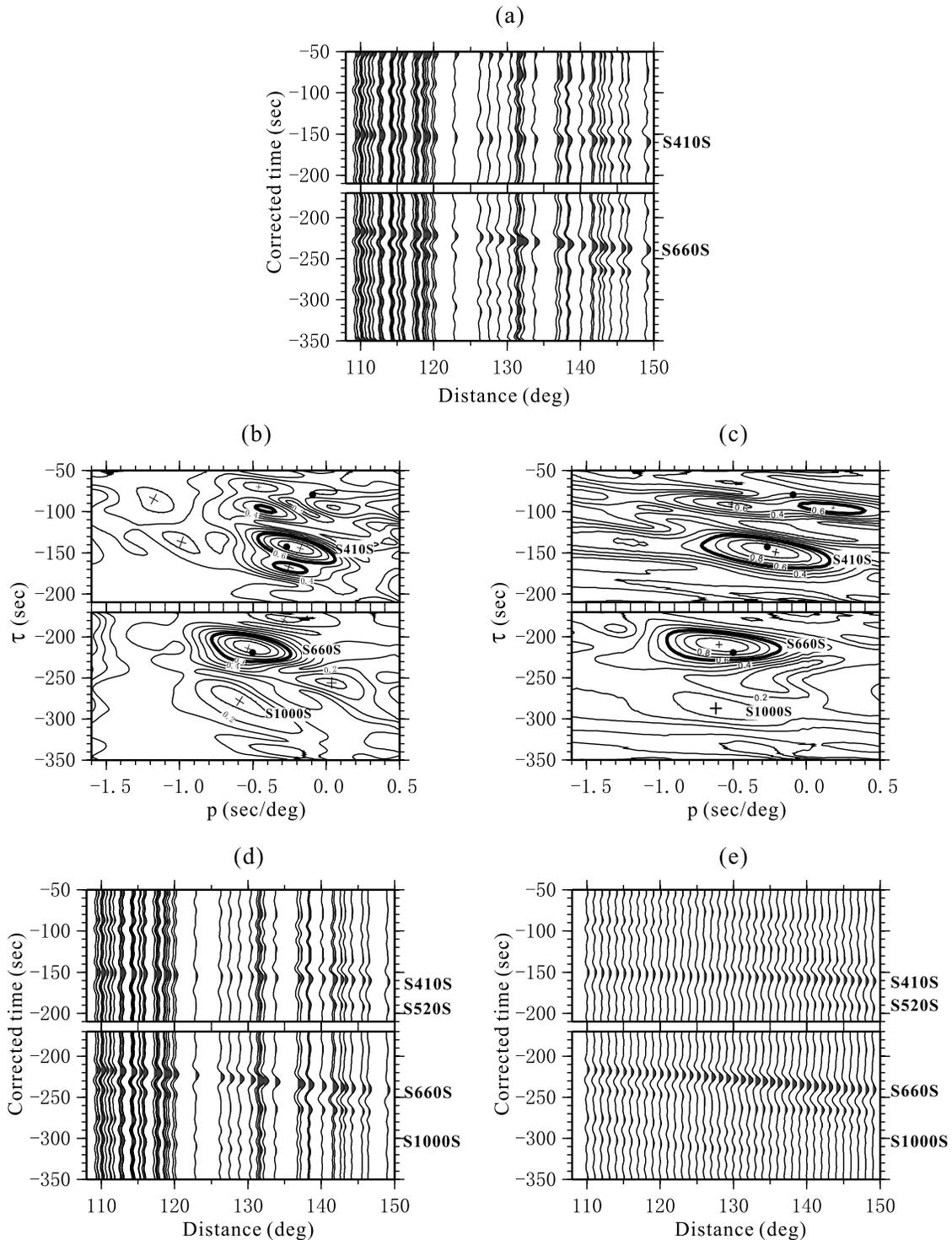
Figure 6. (a) The same time series as Figure 5a after partial stacking (20°) along theoretical ray parameter calculated from PREM for S660S and S410S. (b) The Radon-domain signals of the partially stacked data based on LSRT. (c) The Radon signals of the same data set computed from time domain slant stacks. (d) The reconstructed time series without resampling. (e) The reconstructed time series after resampling and interpolation.

continuity generally shows weak topography except at cap 6, where a pronounced local elevation is observed. The surface of the 660-km discontinuity appears to be more undulating [e.g., *Flanagan and Shearer*, 1998; *Gu et al.*, 1998, 2003],

in particular, the maximum elevation of 33 km under the northeastern Pacific Ocean is not reported by earlier studies of *SS* or *PP* precursors [*Flanagan and Shearer*, 1999; *Deuss et al.*, 2006]. We attribute some of the differences between

Table 1. The Statistics Information of Seven Caps

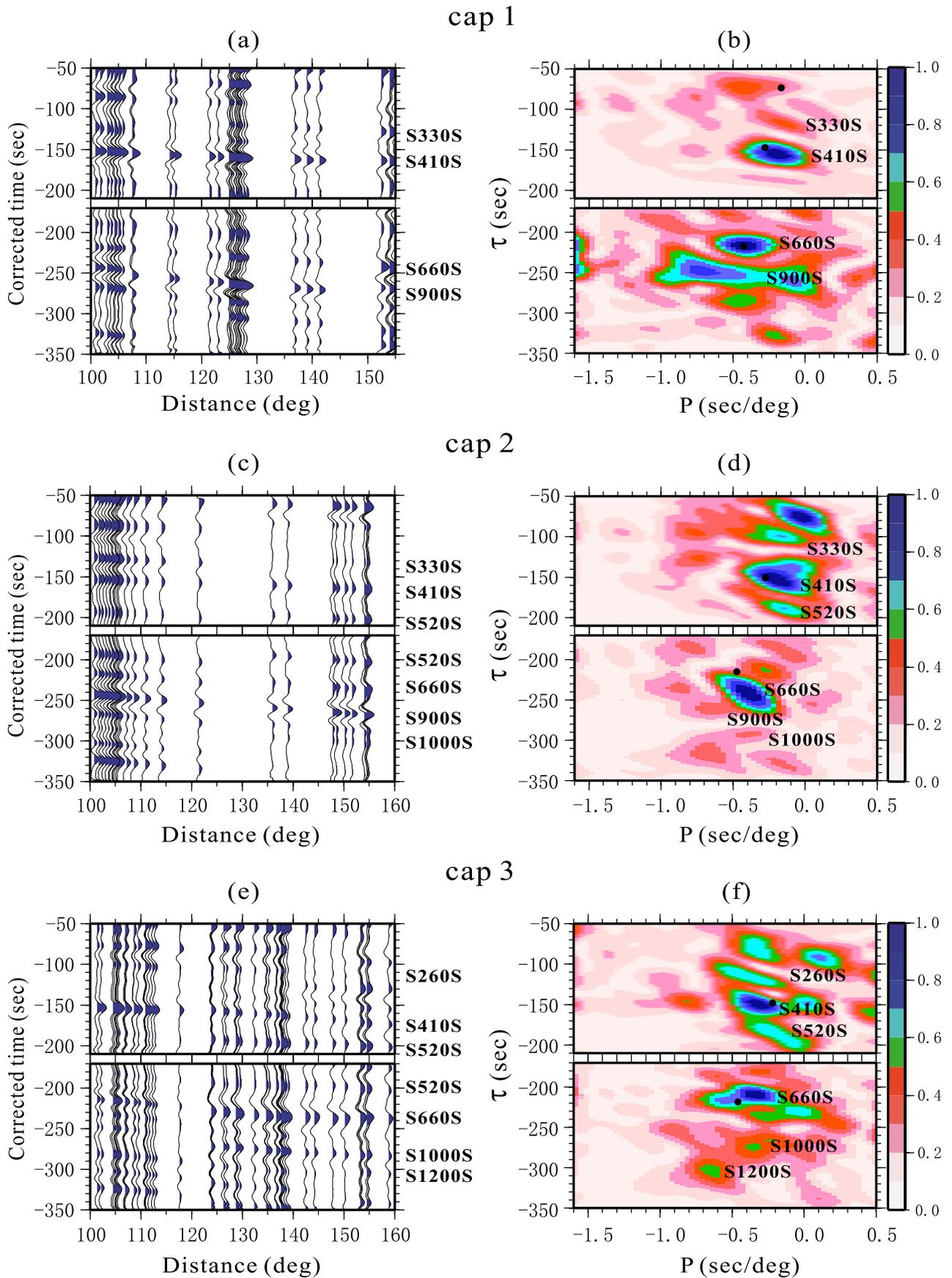|	Location Latitude	Location Longitude	Trace number		S660S Tau (sec)	S660S P (sec/deg)	S660S Depth, km	S660S Deviation, km	S410S Tau, s	S410S P, sec/deg	S410S Depth, km	S410S Deviation, km	TZ thickness, km
Cap 1	42.098	−155.335	36	syn	−217.40	−0.426			−147.11	−0.278	415	0.40	252.00
				data	−216.98	−0.440	667	2.36	−155.15	−0.213			
				mean	−216.80	−0.443			−154.67	−0.225			
				deviation	4.14	0.040			0.91	0.012			
Cap 2	46.630	−152.378	27	syn	−215.09	−0.474			−150.82	−0.277	418	0.62	240.00
				data	−213.09	−0.445	658	0.89	−154.04	−0.214			
				mean	−210.77	−0.432			−152.68	−0.240			
				deviation	4.33	0.027			3.69	0.038			
Cap 3	51.072	−148.884	57	syn	−218.27	−0.461			−148.05	−0.263	419	1.20	229.00
				data	−210.75	−0.349	647	1.30	−150.06	−0.333			
				mean	−209.32	−0.419			−148.79	−0.282			
				deviation	0.60	0.024			1.91	0.040			
Cap 4	55.388	−144.660	70	syn	−219.00	−0.447			−151.59	−0.238	420	1.43	214.00
				data	−211.94	−0.488	634	2.67	−154.15	−0.266			
				mean	−211.74	−0.498			−153.97	−0.256			
				deviation	2.13	0.030			1.10	0.018			
Cap 5	59.523	−139.424	95	syn	−217.75	−0.400			−147.87	−0.189	419	1.49	229.00
				data	−214.28	−0.427	648	1.57	−156.12	−0.212			
				mean	−212.51	−0.441			−148.97	−0.273			
				deviation	4.21	0.033			6.17	0.053			
Cap 6	63.392	−132.779	57	syn	−215.99	−0.406			−143.83	−0.218	391	1.45	252.00
				data	−210.66	−0.427	643	1.52	−143.30	−0.335			
				mean	−211.52	−0.395			−141.00	−0.300			
				deviation	1.46	0.026			1.01	0.059			
Cap 7	66.859	−124.189	60	syn	−219.03	−0.502			−146.84	−0.226	403	0.90	237.00
				data	−212.96	−0.505	640	1.81	−143.60	−0.206			
				mean	−215.32	−0.485			−142.81	−0.235			
				deviation	1.54	0.036			0.95	0.017			
				Average			648.1	1.73			412.1	1.07	236.14

Figure 7

the present and earlier studies to differences in resolution, because strong topography on lateral scale of $\sim$1000 km scales can be invisible to 10-deg caps (with a nominal resolution of 2000 km) used by the earlier global studies.

[26] It should be noted that the estimated depths from LSRT are generally consistent with those obtained using equation (1), particularly of the 410-km discontinuity. The average difference between these two methods is $\sim$3 km and, despite the significant departures in methodology, the large lateral-scale characteristics of the discontinuities are consistently reported by both methods.

[27] We use a bootstrap resampling algorithm [*Efron and Tibshirani*, 1991] to assess the uncertainties associated with the final τ and p values. For each cap, we randomly select same number traces from the database and perform LSRT. This Radon-based procedure is repeated 200 times to generate a statistically significant distribution. Figure 11a shows the bootstrapped measurements of cap 7: the $\tau - p$ values are generally consistent and form a tight cluster around the mean. The depth uncertainties of 660-km is approximately 1. 81 km (Figures 11b and 11c), which is comparable with estimates from *Gu et al.* [2003]. The depth uncertainties for 410-km discontinuity is approximately 0.90 km (Figures 12d–12e), which is appreciably smaller than the reported value of 1.6 km from *Gu et al.* [2003]. The remaining uncertainties (see Table 1) are generally comparable to or better than earlier *SS* precursor studies.

[28] The most significant topographic results are presented by caps 6 and 4. First, we observe a pronounced elevation of 410-km discontinuity beneath the northwestern Canada (cap 6). The discontinuity depth of 391 km is $\sim$20 km shallower than our regional depth average (412.5 km). If we remove the measurement from cap 6, which is the extreme value, the regional average would become $\sim$416 km. The depth of 660-km discontinuity at the same location is 643 km, which is close to the regional average (647 km). A strongly elevated 410-km and a weakly elevated 660-km discontinuities leads to a 10-km thicker TZ than the global average of 242 km [*Gu et al.*, 1998]. The TZ thickness uncertainty in this region is $\sim$2 km, which is too small to account for the observed anomaly. The implications of this TZ structure will be discussed in detail in section 5.

[29] The second significant finding is the elevation of 660-km discontinuity at cap 4, beneath the northeastern Pacific Ocean. The depth of 634 km is 13 km shallower than the regional depth average of 647 km, and is more than 16 km shallower than the global average values reported by earlier studies of *SS* precursors [e.g., *Gu et al.*, 1998; *Flanagan and Shearer*, 1998]. The 410-km discontinuity at the same location is at 420 km, which is slightly deeper than the regional average. Again, these measurements have small uncertainties (1.0–2.7 km) and the observed narrow TZ in this region appears to be well resolved.

4.3. Other Mantle Reflectors

[30] While the presence of the 410- and 660-km discontinuities is well established by global and regional studies, the existence of lithospheric [e.g., *Lehmann*, 1959; *Revenaugh and Jordan*, 1991; *Vidale and Benz*, 1992; *Thybo et al.*, 1997; *Gu et al.*, 2001], 250–330 km [*Revenaugh and Jordan*, 1991; *Deuss and Woodhouse*, 2002], 520-km [e.g., *Shearer*, 1993; *Gu et al.*, 1998; *Deuss and Woodhouse*, 2001] and midmantle discontinuities [*Niu and Kawakatsu*, 1997; *Vinnik et al.*, 2001; *Shen et al.*, 2003] have been much debated during the past few decades. By combining careful data selection with strong constraints in the Radon domain, we are able to confidently resolve some of the aforementioned discontinuities/reflectors beneath the study region (see Table 2 and Figure 11). Figure 11 shows the well-determined reflectors beneath the study transect. The symbol size indicates the clarity of detection of that mantle discontinuity.

[31] Above the TZ, we find little evidence for a significant seismic discontinuity between 180 km and 240 km (see Figures 7 and 8). Even cap 2, the lone location showing a $\tau - p$ peak in the projected Radon domain, is marred by relatively poor spatial data coverage (see Figure 7). However, underside reflections at depths between 250 and 330 km are observed at caps 1–5. The reflections from caps 1 and 5 are more pronounced, as indicated by focused Radon maxima (Figures 7a–7b and 8c–8d), and the migrated depths are 318 and 333 km, respectively. The Pacific upper mantle contains a weak reflector close to 250-km (see caps 2–4) that, judging from the lateral coherence, could be quantified as a regional seismic discontinuity.

[32] Imaging seismic discontinuities within the TZ is often difficult, especially in the time domain, due to large sidelobes of the reflections from 410- and 660-km discontinuities [*Shearer*, 1990; *Shearer*, 1996; *Gu et al.*, 1998]. *Flanagan and Shearer* [1998] proposed a global 520-km discontinuity, but they claimed that reliable observations critically depend on spatial data coverage. In this study, we improve the constraint on this potential discontinuity from both time and Radon domains. We consistently identify a mid-TZ discontinuity (Figure 11), most notably beneath the Pacific Ocean [*Gu et al.*, 1998; *Deuss and Woodhouse*, 2001]. The continental portion of the transect, for example, caps 6 and 7, shows significant complexity. The amplitude of the signal is only slightly above our detection threshold. The topography of the 520-km discontinuity slightly correlates with that of the 660-km discontinuity. The range of depth perturbation is 46 km (524–570 km) and the mean value is 551.4 km; the latter estimate is visibly deeper than the global mean (515 km) reported by *Flanagan and Shearer* [1998]. We do not witness significant splitting of this reflector [*Deuss and Woodhouse*, 2001].

[33] Perhaps the most intriguing result from our regional mapping of mantle discontinuities is the detection of consistent mid/lower mantle reflectors. We use the term "reflector" to indicate that the nature of these reflections may not be global or horizontal. One or multiple underside reflections are consistently observed along the transect (Figure 11 and Table 2), which we associate with previously reported discontinuities at 900, 1050 and 1150 km [*Niu and*

Figure 7. Time series after partial stacking are shown on the left-hand side and the corresponding Radon-domain signal are shown by the right column. The black dots in (b), (d) and (f) denote the theoretical $\tau - p$ values measured from synthetic Radon signals.
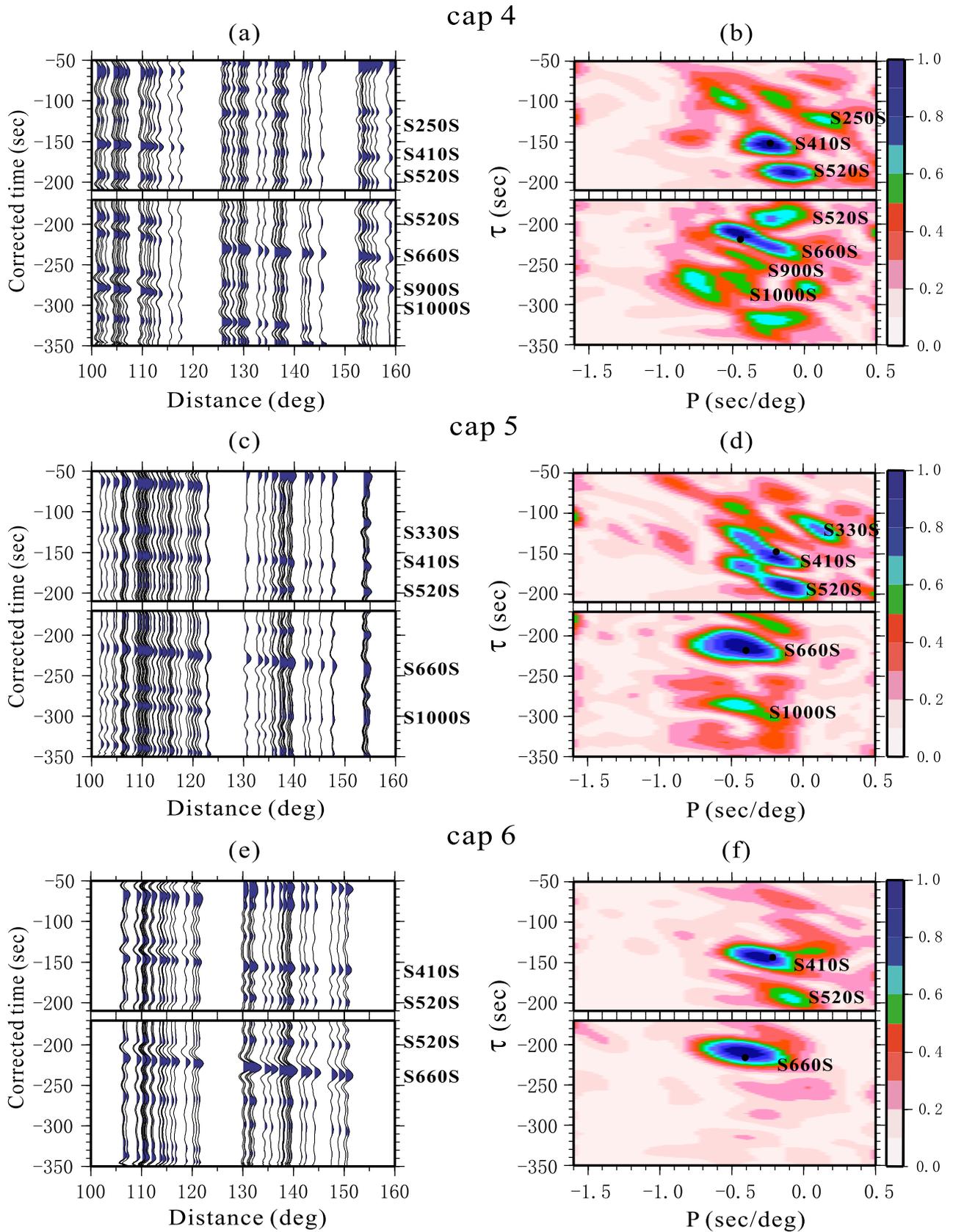
Figure 8. Time series and Radon signals for caps 4–6. The color conventions are the same as those in Figure 7.
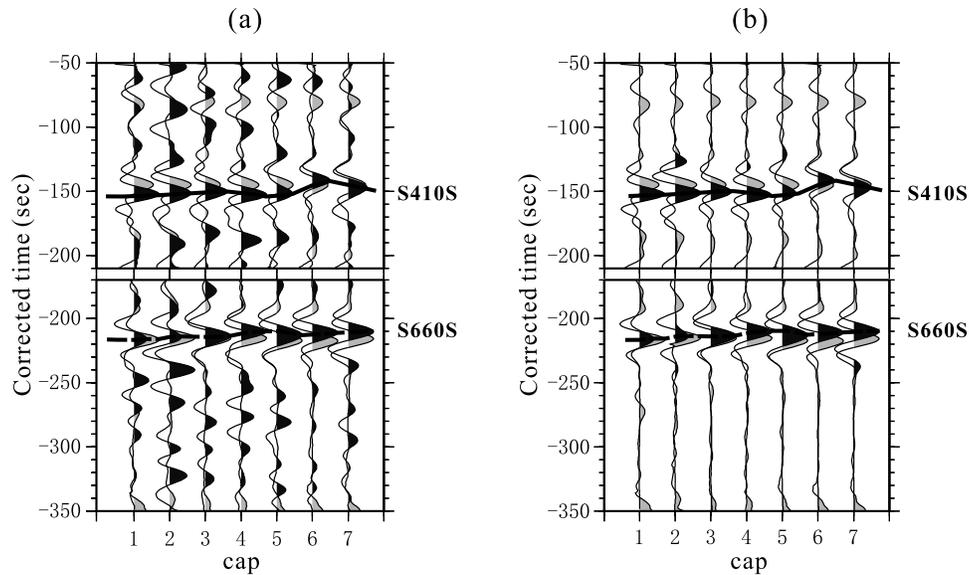
Figure 9. Cumulative stack for each cap based on the measured ray parameter (p) for both synthetic (shown in grey) and observation seismograms (shown in black). To reduce inaccuracies in the stacking procedure, we perform stacking individually for S410S and S660S in each case. The two panels show the stacking results (a) without Radon-domain windowing (post-conditioning), and (b) with Radon-domain windowing.

Kawakatsu, 1997; *Deuss and Woodhouse*, 2002]. For example, a reliably detected reflector is present at ∼1000 km at cap 3 and cap 5. The lateral coherence of these reflectors has significant implications for the thermal and compositional variations above and within the mid mantle (see discussions).

5. Discussion

[34] A distinct advantage of LSRT over traditional approaches is its ability to constrain differential ray parameter and traveltime simultaneously. Combined with the effective removal of correlated/random noise through post-conditioning in the Radon domain, LSRT can accurately determine the topography of known TZ discontinuities and detect weak mantle reflectors.

[35] First, the depth and reflectivity of TZ discontinuities impose indirect constraints on the thermal and potential compositional variations. It is often assumed that solid-solid phase transitions from α-olivine to β-wadsleyite and from γ-ringwoodite to magnesiowüstite [(Fe, Mg)O] and silicate perovskite [(Mg, Fe)SiO$_3$] [*Ringwood*, 1975; *Ito and Takahashi*, 1989] are mainly responsible for the respective velocity changes at depths near 410 and 660-km. Then, a significantly shallower 410-km discontinuity near northern British Columbia (at cap 6) would, in the absence of compositional changes, suggest a colder-than-normal mantle due to the positive Clapeyron slope of the former transition [*Katsura and Ito*, 1989]. If we assume the Fo90 composition [*Katsura and Ito*, 1989], an elevation of ∼30 km at this cap location would translate into a temperature difference in excess of 250°C relative to the ambient mantle. An anomaly of such magnitude is unlikely an artifact of inaccurate mantle velocity corrections, nor could it be caused by horizontal smearing of present-day seismic
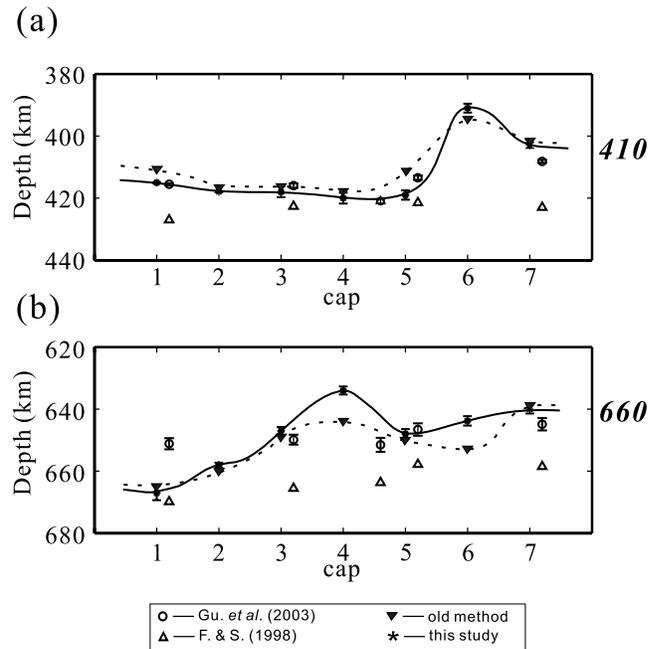

Figure 10. TZ discontinuities depths. In each case, the stars represent the final depth measurements of this study. F. & S. — *Flanagan and Shearer* [1998]. The stars represent the depth measurements obtained from LSRT and, the inverted triangles represent those obtained from equation (1). (a) The depth of 410-km discontinuity. (b) The depth of 660-km discontinuity. The topography maps are generally consistent, especially of the 410-km discontinuity. However, the smaller-scale topography observed by this study, for example, at caps 4 and 6, are not present in the earlier studies.
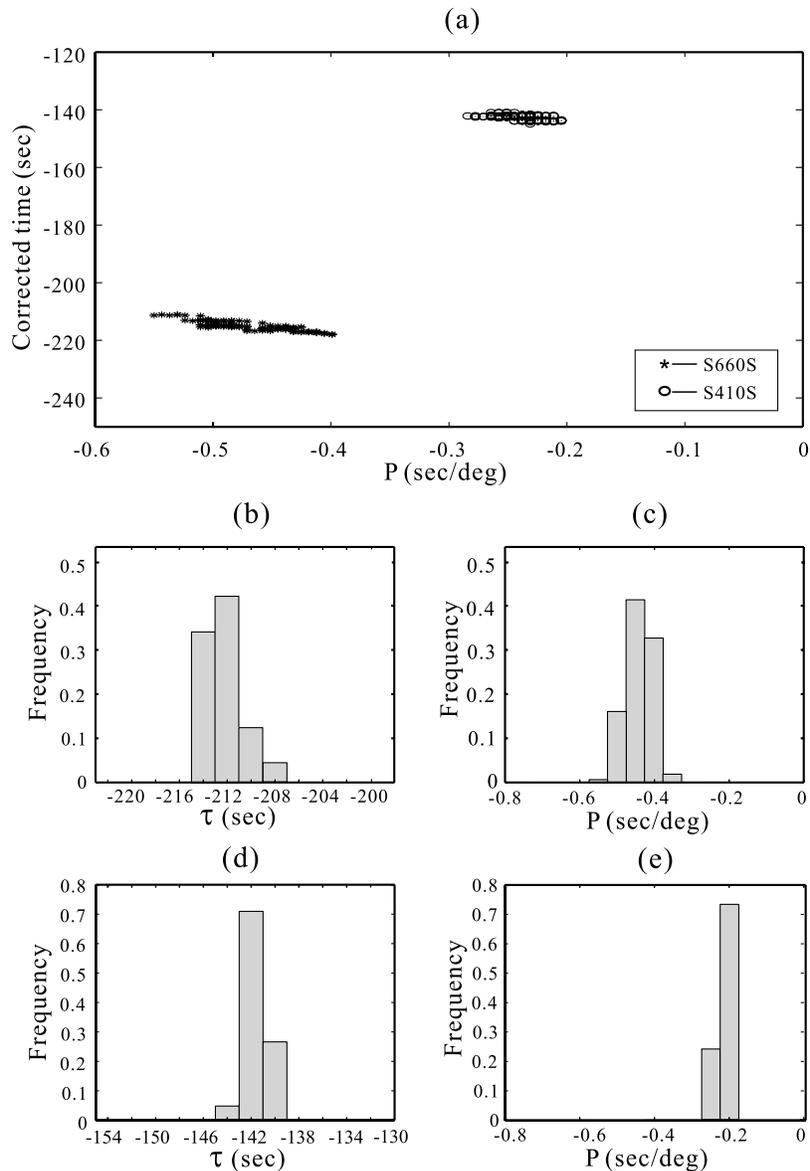
Figure 11. (a) Bootstrapped Radon-domain measurements of S410S and S660S at cap 7. The histograms show the distribution of measurements for (b) the τ value of S660S, (c) the p value of S660S, (d) the τ value of S410S, and (e) the p value of S410S.

structures more than 1500 km away from its cap center; the Fresnel-zone volume of the SS precursors is ∼1000– 1500 km [*Neele et al.*, 1997; *Shearer et al.*, 1999]. Considering the history of this region and its proximity to major subduction zones northwest (near the eastern Aleutian trench) and south (due to the interaction of Kula, Farallon-Pacific and North America Plates), a remnant part of the subducted oceanic lithosphere in the TZ may be responsible for the observed topography. In particular, the Farallon-Pacific spreading center approached the Farallon-North America subduction zone at 50–55 Ma [*Stock and Molnar*, 1988; *Braunmiller and Nabelek*, 2002]. The plate convergence and the subsequent subduction nearly deposited the entire lithosphere of the former Kula-Farallon plates into the mantle beneath western North America. Part of the high-velocity lithosphere has potentially reached

midmantle [*Grand et al.*, 1997; *Kárason and van der Hilst*, 1998; *Bunge and Grand*, 2000], while remaining traces of the slab material may have been littered throughout the mantle beneath North America. We hypothesize that a fraction of the substantial mass flux from the series of subduction events remained in the upper mantle and contribute to the high velocities observed at ∼391-km depth north of the present-day Cascadian subduction zone. The northward extension of the subduction slab is quite possible in this tectonically complex region, considering that the remnant Farallon plate at midmantle depths nearly span the entire North American plate along a northwest-southeast orientation, as evidenced by high-resolution P and S wave tomography [e.g., *Kárason and van der Hilst*, 1998; *Boschi and Dziewonski*, 2000]. The presence of a fast upper-mantle velocity beneath cap 6 is also consistent with results
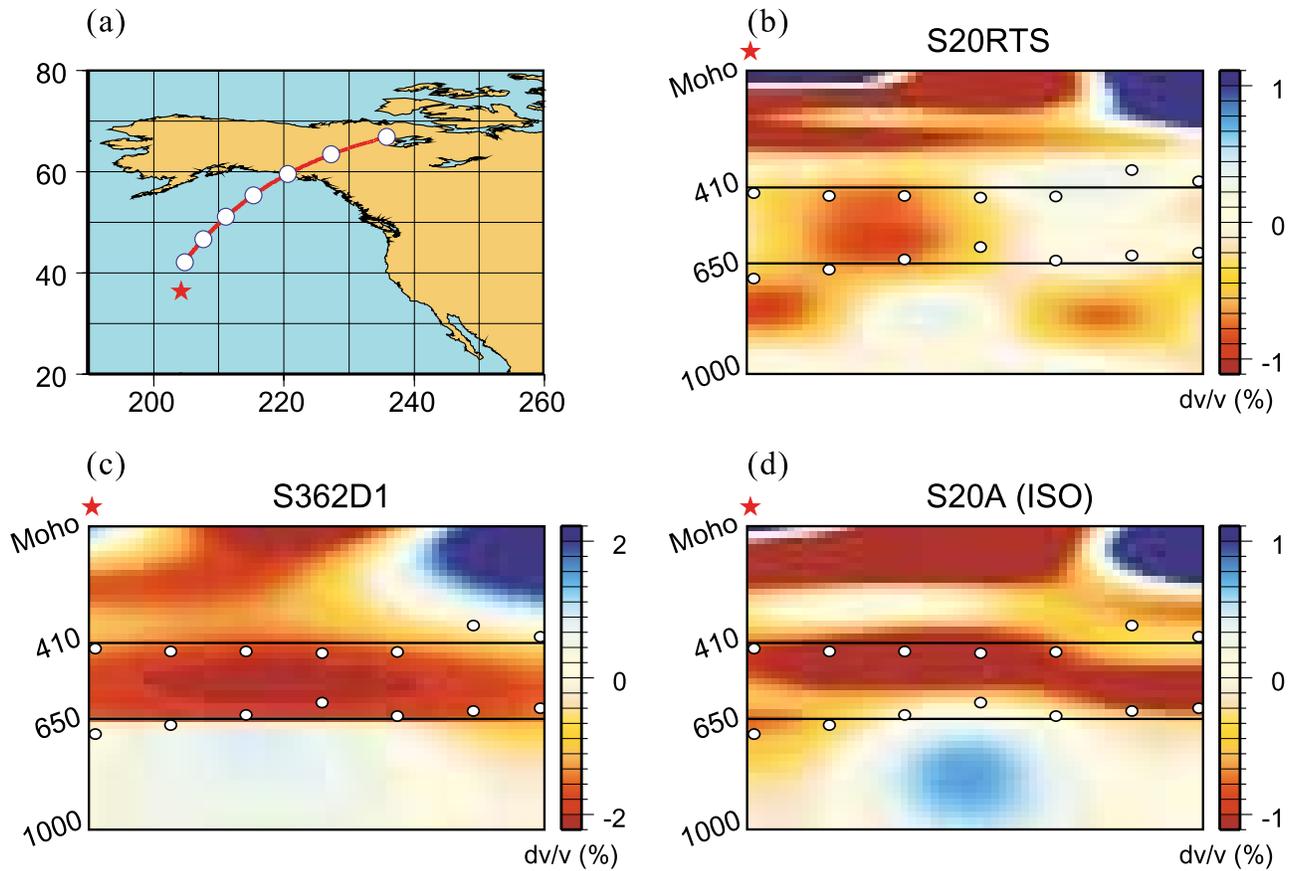
Figure 12. A comparison of discontinuity depth and mantle shear velocity. (a) The locations of cap centers. The tomographic models are (b) S362D1 [*Gu et al.*, 2003], (c) S20A [*Ekström and Dziewonski*, 1998], and (d) S20RTS [*Ritsema et al.*, 1999]. The location of the anomalously thin TZ beneath the northeastern Pacific Ocean appears to coincide with a low-velocity TZ anomaly in the tomographic models.

obtained by recent high-resolution *S*-wave tomographic models of *Bunge and Grand* [2000].

[36] Should the aforementioned high-velocity anomaly continue across the 660-km discontinuity, one would expect the 660-km discontinuity to be locally depressed due to the endothermic nature of the γ -phase phase transition. However, despite a thickened TZ, the topography of the 660-km discontinuity is slightly elevated (to 643 km)

instead. The lack of anti-correlation between the 410- and 660-km discontinuities could suggest: 1. the proposed high velocity anomaly terminates within the transition zone, or 2. the proposed high velocity anomaly continues down to the lower mantle, but the presence of compositional variations and/or other phase transitions sufficiently counteracts the thermal effects on the olivine phase transition. The first scenario could materialize if the high velocity region

Table 2. The Detection of Other Mantle Discontinuities

		Depth, km						
Discontinuities		Cap 1	Cap 2	Cap 3	Cap 4	Cap 5	Cap 6	Cap 7
220 km	no evidence	*a			*	*	*	*
	weak		*	*				
	detected							
250–330 km	no evidence						*	*
	weak		318	268		253		
	detected	318				333		
520 km	no evidence	*						
	weak						570	524
	detected		554	532	547	562		
800–1100 km	no evidence						*	
	weak	860	860 961	1028	955 1055			1027
	detectable			1198		1055		

a * Represents no detection of discontinuities.
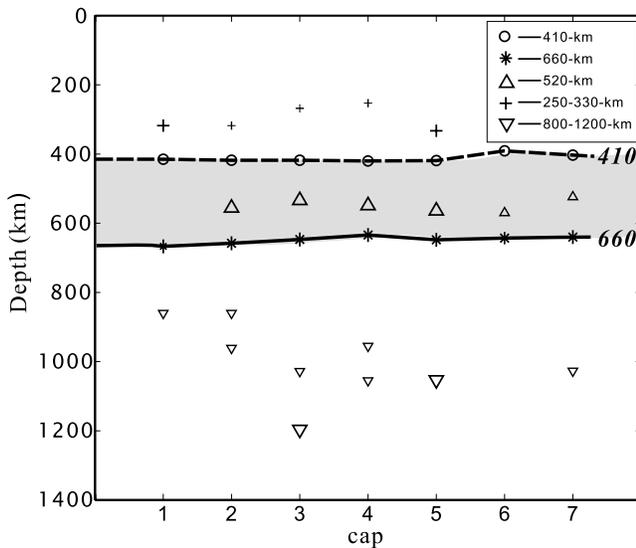
Figure 13. Detected mantle discontinuities/reflectors down to mid-mantle depths. The symbol size corresponds to the quality of measurements and reliability of detection. The X discontinuities are detectable at most cap locations. The 520-km discontinuity is generally observed below 530 km, and a series of mid-mantle reflectors are detected.

represents a broken piece of subducted oceanic lithosphere near the 410-km discontinuity. Local compositional variations near the 660-km discontinuity can just as easily reduce the seismic velocities and elevate the phase boundary, for example, through an increase of Fe and/or water content [*Sinogeikin et al.*, 1998; *Katsura et al.*, 2004; *Yusa and Inoue*, 1997; *Chen et al.*, 2002; *Bercovici and Karato*, 2003]. Furthermore, phase transition of majoritic garnet to Ca-perovskite [*Weidner and Wang*, 2000; *Hirose*, 2002; *Deuss et al.*, 2006], an exothermic process, could overcome the effect of the endothermic olivine phase transition near 660 km. The separation of thermal versus compositional variations from the limited seismic data is difficult without further data constraint.

[37] The second significant feature of the two major TZ discontinuities is the combination of a depressed 410-km discontinuity and an elevated 660-km discontinuity beneath the northern Pacific (see caps 4–6). The opposite movement of the phase boundaries and a thin TZ can be caused by a low temperature anomaly penetrating the TZ. If we assume a thermal origin, the TZ thickness in this region (214 km) would translate into a temperature difference of ~150°C relative to that of an average TZ mantle. The presence of the proposed low-velocity zone in this region is supported by recent tomographic models (Figure 13). For example, corresponding cross-sections of S20RTS [*Ritsema et al.*, 1999], S362D1 [*Gu et al.*, 2003] and S20A [*Ekström and Dziewonski*, 1998] consistently show a TZ low-velocity zone in the northeastern Pacific, generally coinciding with the thinnest part of the TZ in our study region. Judging from the results of tomographic models, this anomaly has a lateral dimension of 1500–2500 km and covers a significant portion of the northeastern Pacific Ocean. The origin of the Pacific heterogeneity is unknown since the center

location is relatively far from major subduction zone (in the northeast) or potentially deep-rooted hot spot (in the southwest) locations. Thermal effect aside, a vertical structure with minor variations in Fe content [*Sinogeikin et al.*, 1998; *Katsura et al.*, 2004] or the presence of H_2O/melt [*Yusa and Inoue*, 1997; *Chen et al.*, 2002] could offer alternative explanations for the observed phase boundary perturbations.

[38] Besides the well-known phase boundaries, the improved accuracy and resolution of the LSRT approach enable a closer examination of intermittently reported reflectors in the mantle. We started with the Lehmann discontinuity [*Lehmann*, 1959] between 180–240 km depth ranges. Since the incorporation of this discontinuity as a global interface [*Dziewonski and Anderson*, 1981], a number of studies have provided regional evidence for the 220-km discontinuity beneath stable Cratons [*Gaherty and Jordan*, 1995; *Gu et al.*, 2001; *Duess and Woodhouse*, 2002] and plate-boundary zones [*Revenaugh and Jordan*, 1991; *Vidale and Benz*, 1992; *Gu et al.*, 2005]. However, the global existence of this discontinuity is still in question [*Shearer*, 1993; *Gossler and Kind*, 1996; *Gu et al.*, 1998; *Flanagan and Shearer*, 1998]. With the exceptions of caps 3 and 4, where a reflection is barely recognizable between 20–240 km, we do not find evidence for significant energy peaks in the Radon domain that could be associated with a mechanical or thermal boundary layer. The lack of a robust 220-km discontinuity beneath the Pacific Ocean is not unexpected, as the shallower Gutenberg discontinuity at ~160-km depth may represent the true lithosphere-asthenosphere boundary [e.g., *Gung et al.*, 2003]. The incoherent S220S signal beneath the western North America at high latitudes (caps 6–8) is surprising, despite recent observations of weak or complex secondary reflections/conversions associated with the base of lithosphere [*Gu et al.*, 2001; *Deuss and Woodhouse*, 2002]. We believe that strong local-scale topographic variations similar to an eastward dip reported beneath Vancouver Island [*Bostock*, 1996] may be responsible. Still, judging from individual long-period records, the presence of a *laterally coherent* 220-km discontinuity is unlikely beneath the profile examined in this study.

[39] We do identify, however, reflectors at moderately deeper depths (250–330 km) at most cap locations. Their presence is evidenced by one (or more) consistent distance-time move out(s) between SS and S410S after eliminating topside reflections and crustal multiples. Similar phases have been documented by *Deuss and Woodhouse* [2002] using a time domain analysis beneath the Pacific Ocean and were attributed to the presence of X discontinuities [*Revenaugh and Jordan*, 1991; *Li and Fischer*, 2002; *Williams and Revenaugh*, 2005]. Without consistent depth variations across the transect, it is difficult to assess whether the cause of these discontinuities represent potential phase changes in the coesite to stishovite system, exsolution of stishovite from clinopyroxenes [*Williams and Revenaugh*, 2005] or, in some cases, simply a deeper lithospheric discontinuity.

[40] In addition to X discontinuities, we find clear evidence for a weak reflector within the transition zone [e.g., *Gu et al.*, 1998; *Flanagan and Shearer*, 1998; *Deuss and Woodhouse*, 2001]. The former discontinuity was first

reported by *Shearer* [1990, 1996] as a global feature, and has since been associated with either an endothermic phase change between β-wadsleyite and γ-ringwoodite [*Ringwood*, 1975] or phase changes in the garnet system [*Weidner and Wang*, 2000; *Deuss and Woodhouse*, 2001]. Along the transect examined in this study, a positive phase with a similar move out curve as $S660S$ strongly suggests the presence of a secondary velocity jump within the transition zone. The consistent timing of the signal over several caps argues against the effect of random scattering within a laterally heterogeneous mantle. We do not observe two distinct discontinuities within the transition zone beneath continental regions, though the reflection amplitude of the lone discontinuity is visibly lower than that beneath the oceans [*Deuss and Woodhouse*, 2001].

[41] Finally, the improvement in resolution (with 5-deg caps) and methodology enables a more accurate assessment of potential lower/mid mantle reflectors. Reflectors at depths below 660 km have been previously identified beneath subduction zones [*Karakatsu and Niu*, 1994; *Niu and Kawakatsu*, 1997; *Vinnik et al.*, 2001], and were attributed to the effect of subducted oceanic lithosphere in the lower mantle. Furthermore, *Shen et al.* [2003] identified a lower-mid mantle reflector around 1050 km beneath the South Pacific Superswell, a hot spot location, and attributed to the mineralogical phase transition at the upper-lower mantle. *Wen and Anderson* [1995] suggested that a partial flow barrier may exist near 900 km as the result of chemical differentiation. In this study, one or more lower mantle reflector(s) is consistently present beneath the cap locations, though their lateral depth variations across the entire profile (over 400 km) are too great to be accounted for by the topography of a single, regional discontinuity. Our results suggest that lower mantle reflectors are more common than were suggested previously and their origins and depths could vary greatly. In other words, both thermal and compositional variations could contribute to their presence. A satisfactory interpretation of these midmantle reflectors remains a work in progress.

6. Conclusions

[42] This is a pilot study of the upper mantle discontinuities using LSRT, a high-resolution approach that simultaneously constrain differential time and ray parameter. The use of least squares Radon transform greatly improves the resolution and flexibility over time domain approaches such as slowness stacking. LSRT also enables a full reconstruction of the original time series after regularization and slowness windowing. In other words, it can be used as an effective de-noising and interpolating tool.

[43] By means of Radon transform, we infer the depth of mantle discontinuities from the differential traveltimes of long-period SS and its precursors. In addition to a consistent 520-km discontinuity across the study region, two key observations regarding the upper mantle TZ stand out: 1) a strong elevation of the 410-km discontinuity and a normal 660-km discontinuity beneath northwestern Canada, and 2) a narrow TZ beneath the northeastern Pacific Ocean. The first observation may be evidence of subducted oceanic lithosphere in the transition zone due to past interactions of Kula, Farallon, and North America plates. Still, potential

compositional variations and garnet-perovskite phase transformations could be important near the 660-km depths in the region. The narrow TZ beneath the northeastern Pacific is most likely caused by a low-velocity heterogeneity penetrating the TZ.

[44] We also successfully identified several upper- (X) and midmantle discontinuities, but we failed to find convincing evidence for a lithospheric discontinuity between 180 and 240 km. More work remains to be done to truly understand the nature of these secondary discontinuities/reflectors in the mantle. A greater data density and wider data coverage, as well as higher resolution methods, would undoubtedly aid that effort. Fortunately, with little modification, the LSRT approach outlined in this study can be equally effective for global and regional analysis of PP precursors, ScS reverberations, converted waves (receiver functions) and, virtually, all other array techniques employed in mantle imaging.

References

Agee, C. B., and D. Walker (1988), Olivine flotation in mantle melt, *Earth Planet. Sci. Lett.*, *90*, 144–156.

Bassin, C., and G. Laske (2000), The current limits of resolution for surface wave tomography in North America, *Eos Trans. AGU*, *81*, Fall. Meet. Suppl. F897.

Bercovici, D., and S. Karato (2003), Whole-mantle convection and the transition-zone water filter, *Nature*, *438*, 39–44.

Boschi, L., and A. M. Dziewonski (2000), Whole Earth tomography from delay times of P, PcP, and PKP phases: Lateral heterogeneity in the outer core or radial anisotropy in the mantle?, *J. Geophys. Res.*, *105*, 13,675–13,696.

Bostock, N. G. (1996), Ps conversions from the upper mantle transition zone beneath the Canadian landmass, *J. Geophys. Res.*, *101*, 8393–8402.

Braunmiller, J., and J. Nabelek (2002), Seismotectonics of the Explorer region, *J. Geophys. Res.*, *107*(B10).

Bunge, H. P., and S. P. Grand (2000), Mesozoic plate-motion history below the northeast Pacific Ocean from seismic images of the subducted Farallon slab, *Nature*, *405*(18), 337–340.

Chambers, K., J. H. Woodhouse, and A. Deuss (2005), Topography of the 410-km discontinuity from PP and SS precursors, *Earth Planet. Sci. Lett.*, *234*, 610–622.

Chen, J., T. Inoue, H. Yurimoto, and D. J. Weidner (2002), Effect of water on the olivine-wadsleyite phase boundary in the $(Mg, Fe)_2SiO_4$ system, *Geophys. Res.*, *29*.

Deuss, A., and J. H. Woodhouse (2001), Seismic observations of splitting of the mid-transition zone discontinuity in the Earth's mantle, *Science*, *294*, 354–357.

Deuss, A., and J. H. Woodhouse (2002), A systematic search for mantle discontinuities using SS-precursors, *Geophys. Res. Lett.*, *29*, x-1–x-4.

Deuss, A., S. A. T. Redfern, K. Chambers, and J. H. Woodhouse (2006), The nature of the 660-km discontinuity in Earth's mantle from global seismic observations of PP precursors, *Science*, *311*, 198–201.

Dziewonski, A. M., and D. L. Anderson (1981), Preliminary reference Earth model, *Phys. Earth Planet. Inter.*, *25*, 297–356.

Efron, B., and R. Tibshirani (1991), Statistical data analysis in the computer age, *Science*, *253*, 390–395.

Ekström, G., and A. M. Dziewonski (1998), The unique anisotropy of the Pacific upper mantle, *Nature*, *394*, 168–172.

Engl, H. W., and W. Grever (1994), Using the L-curve for determining optimal regularization parameters, *Numer. Math.*, *69*, 25–31.

Flanagan, M. P., and P. M. Shearer (1998), Global mapping of topography on transition zone velocity discontinuities by stacking SS precursors, *J. Geophys. Res.*, *103*, 2673–2692.

Flanagan, M. P., and P. M. Shearer (1999), A map of the topography on the 410-km discontinuity from PP precursors, *Geophys. Res. Lett.*, *26*, 549–552.

Foster, J. D., and C. C. Mosher (1992), Suppression of multiple reflections using the Radon Transform, *Geophysics*, *57*(3), 386–395.

Gaherty, J., and T. H. Jordan (1995), Lehmann discontinuity as the base of an anisotropic layer beneath continents, *Science*, *268*, 1468–1471.

Gossler, J., and R. Kind (1996), Seismic evidence for very deep roots of continents, *Earth Planet. Sci. Lett.*, *138*(1-4), 1–13.

Grand, S. P., R. D. van der Hilst, and S. Widiyantoro (1997), Global seismic tomography: A snapshot of convection in the Earth, *GSA Today*, *7*, 1–7.

Gu, Y. J., and A. M. Dziewonski (2002), Global variability of transition zone thickness, *J. Geophys. Res.*, *107*(B7).

Gu, Y. J., A. M. Dziewonski, and C. B. Agee (1998), Global de-correlation of the topography of transition zone discontinuities, *Earth Planet. Sci. Lett.*, *157*, 57–67.

Gu, Y. J., A. M. Dziewonski, and G. Ekström (2001), Preferential detection of the Lehmann discontinuity beneath continents, *Geophys. Res. Lett.*, *28*, 4655–4658.

Gu, Y. J., A. M. Dziewonski, and G. Ekström (2003), Simultaneous inversion for mantle shear velocity and topography of transition zone discontinuities, *Geophys. J. Int.*, *154*, 559–583.

Gu, Y. J., A. L. Lerner-Lam, A. M. Dziewonski, and G. Ekström (2005), Deep structure and seismic anisotropy beneath the East Pacific Rise, *Earth Planet. Sci. Lett.*, *232*, 259–272.

Gung, Y., M. Panning, and B. Romanowicz (2003), Global anisotropy and the thickness of continents, *Nature*, *422*, 707–711.

Hampson, D. (1986), Inverse velocity stacking for multiple elimination, *56th Ann. Internat. Mtg., Soc. Expl. Geophys.*, Expanded Abstracts, 422–424.

Hirose, K. (2002), Phase transitions in pyrolitic mantle around 670-km depth: Implications for upwelling of plumes from the lower mantle, *J. Geophys. Res.*, *107*(B4).

Ito, E., and E. Takahashi (1989), Postspinel transformations in the system Mg_2SiO_4-Fe_2SiO_4 and some geophysical implications, *J. Geophys. Res.*, *94*, 10,637–10,646.

Kárason, H., and R. D. van der Hilst (1998), Improving seismic models of whole mantle P-wave speed by the inclusion of data from differential times and normal modes, *EOS, Trans. Am. Geophys. Un.*, *79*(45), Fall Mtg Suppl., F656.

Katsura, T., and E. Ito (1989), The system $Mg_2S_iO_4$-$Fe_2S_iO_4$ at high pressures and temperatures: Precise determination of stabilities of olivine, modified spinel, and spinel, *J. Geophys. Res.*, *94*, 15,663–15,670.

Katsura, T., H. Yamada, O. Nishikawa, M. Song, A. Kubo, T. Shinmei, S. Yokoshi, Y. Aizawa, T. Yoshino, M. J. Walter, E. Ito, and K. Funakoshi (2004), Olivine-wadsleyite transition in the system $(Mg, Fe)_2S_iO_4$, *J. Geophys. Res.*, *109*, B02209, doi:10.1029/2003JB002438.

Kawakatsu, H., and F. Niu (1994), Seismic evidence for a 920-km discontinuity in the mantle, *Nature*, *371*, 301–305.

Lehmann, I. (1959), Velocities of longitudinal waves in the upper part of the Earth's mantle, *Ann. Geophys.*, *15*, 93–113.

Li, A., and K. M. Fischer (2002), Crust and upper mantle discontinuity structure beneath eastern North America, *J. Geophys. Res.*, *107*(B5), 2100, doi:10.1029/2001JB000190.

Menke, W. (1989), *Geophysical Data Analysis: Discrete Inverse Theory*.

Neele, F., H. de Regt, and J. VanDecar (1997), Gross errors in upper-mantle discontinuity topography from underside reflection data, *Geophys. J. Int.*, *129*(1).

Niu, F., and H. Kawakatsu (1997), Depth variation of the mid-mantle seismic discontinuity, *Geophys. Res. Lett.*, *24*(4), 429–432.

Papoulis, A. (1962), *The Fourier Integral and its Applications*, McGraw-Hill, New York.

Revenaugh, J., and T. H. Jordan (1991), Mantle layering from ScS reverberations 3: The upper mantle, *J. Geophys. Res.*, *96*(B12), 19,781–19,810.

Ringwood, A. E. (1975), *Composition and Petrology of the Earth's Mantle*, 618 pp., McGraw-Hill, New York.

Ritsema, J., H. J. Van Heijst, and J. H. Woodhouse (1999), Complex shear wav velocity structure imaged beneath Africa and Iceland, *Science*, *286*, 1925–1928.

Rost, S., and C. Thomas (2002), Array seismology: Methods and applications, *Rev. Geophys.*, *40*(3), 1–27.

Sacchi, M., and T. Ulrych (1995), High-resolution velocity gathers and offset space reconstruction, *Geophysics*, *60*, 1169–1177.

Schmerr, N., and E. J. Garnero (2006), Investigation of upper mantle discontinuity structure beneath the central Pacific using SS precursors, *J. Geophys. Res.*, *111*, B08305, doi:10.1029/2005JB004197.

Shearer, P. M. (1990), Seismic imaging of upper-mantle structure with new evidence for a 520-km discontinuity, *Nature*, *344*, 121–126.

Shearer, P. M. (1993), Global mapping of upper mantle reflectors from long-period SS precursors, *Geophys. J. Int.*, *115*, 878–904.

Shearer, P. M. (1996), Transition zone velocity gradients and the 520-km discontinuity, *J. Geophys. Res.*, *101*, 3053–3066.

Shearer, P. M., and G. Masters (1992), Global mapping of topography on the 660-km discontinuity, *Nature*, *355*, 791–796.

Shearer, P. M., M. P. Flanagan, and M. A. H. Hedlin (1999), Experiments in migration processing of SS Precursor data to image upper mantle discontinuity structure, *J. Geophys. Res.*, *104*, 7229–7242.

Shen, Y., C. J. Wolfe, and S. C. Solomon (2003), Seismological evidence for a mid-mantle discontinuity beneath Hawaii and Iceland, *Earth Planet. Sci. Lett.*, *214*, 143–151.

Sinogeikin, S. V., T. Katsura, and J. D. Bass (1998), Sound velocities and elastic properties of Fe-bearing wadsleyite and ringwoodite, *J. Geophys. Res.*, *103*, 20,819–20,825.

Stock, J. M., and P. Molnar (1988), Uncertainties and implications of the Cretaceous and Tertiary position of North America relative to Farallon, Kula, and Pacific plates, *Tectonics*, *7*, 1339–1384.

Su, W. J., R. L. Woodward, and A. M. Dziewonski (1994), Degree-12 model of shear velocity heterogeneity in the mantle, *J. Geophys. Res.*, *99*, 6945–6980.

Thybo, H., E. Perchuc, and N. Pavlenkova (1997), Two reflectors in the 400 km depth range revealed from peaceful nuclear explosion seismic sections, in *Upper-Mantle Heterogeneities from Active and Passive Seismology*, pp. 97–104, ed. K. Fuchs, NATO ASI Series, Kluwer, Dordrecht.

Vidale, J. E., and H. M. Benz (1992), Upper-mantle seismic discontinuities and the thermal structure of subduction zones, *Nature*, *356*, 678–683.

Vinnik, L., N. Kato, and H. Kawakatsu (2001), Search for seismic discontinuities in the lower mantle, *Geophys. J. Int.*, *147*, 41–56.

Weidner, D. J., and Y. Wang (2000), Phase transformations: Implications for mantle structure, in *Earth'deep interior: Mineral physics and tomography from the atomic to the global scale*, *Geophys. Monogr. Ser.*, *117*, edited by S. Karato et al., 215–235, AGU, Washington, D. C.

Wen, L., and D. L. Anderson (1995), The fate of slabs inferred from seismic tomography and 130 million years of subduction, *Earth Planet. Sci. Lett.*, *133*, 185–198.

Wessel, P., and W. H. F. Smith (1991), Free software helps map and display data, *Eos Trans. AGU*, *72*, 445–446.

Williams, Q., and J. Revenaugh (2005), Ancient subduction, mantle eclogite, and the 300 km seismic discontinuity, *Geology*, *33*(1), 1–4.

Wilson, C., and A. Guitton (2007), Teleseismic wavefield interpolation and signal extraction using high-resolution linear radon transforms, *Geophys. J. Int.*, *168*, 171–181.

Yusa, H., and T. Inoue (1997), Compressibility of hydrous wadsleyite (β-phase) in Mg2SiO4 by high pressure X-ray diffraction, *Geophys. Res. Lett.*, *24*, 1831–1834.

————————————

Y. An, Y. J. Gu, and M. D. Sacchi, University of Alberta, Physics 11322-89 Avenue Edmonton, Alberta, T6G 2G7, Canada. (yan@phys.ualberta.ca)